Non-unique bubble dynamics in a vertical capillary with an external flow

Journal:	*Journal of Fluid Mechanics*
Manuscript ID	JFM-20-S-0886.R2
mss type:	JFM Papers
Date Submitted by the Author:	n/a
Complete List of Authors:	Yu, Yingxian; Princeton University, Department of Mechanical and Aerospace Engineering Magnini, Mirco; University of Nottingham, Department of Mechanical, Materials and Manufacturing Engineering Zhu, Lailai ; Princeton University, Department of Mechanical and Aerospace Engineering; National University of Singapore, Department of Mechanical Engineering Shim, Suin; Princeton University, Department of Mechanical and Aerospace Engineering Stone, Howard; Princeton University, Department of Mechanical and Aerospace Engineering
Keywords:	Bubble dynamics < Drops and Bubbles, Lubrication theory < Low-Reynolds-number flows
Abstract:	We study bubble motion in a vertical capillary tube under an external flow. Bretherton (1961) showed that, without external flow, a bubble can spontaneously rise when the Bond number ($Bo \equiv \rho g R^2/\gamma$) is above the critical value 0.842. It was then shown by Magnini *et al.* (2019) that the presence of an imposed liquid flow, in the same (upward) direction as buoyancy, accelerates the bubble and thickens the liquid film around it. In this work we carry out a systematic study of the bubble motion under a wide range of external flows, focusing on the inertialess regime with Bo above the critical value. We show that a rich variety of bubble dynamics occur when an external downward flow is applied, opposing the buoyancy-driven rise of the bubble. We reveal the existence of a critical capillary number of the external downward flow ($Ca_l \equiv \mu U_l/\gamma$) at which the bubble arrests and changes its translational direction. Depending on the relative direction of gravity and the external flow, the film thickness follows two distinct solution branches. The results from theory, experiments and numerical simulations confirm the existence of the two solution branches and reveal that the two branches overlap over a finite range of Ca_l, thus suggesting non-unique, history-dependent solutions for the steady-state film thickness under the same external flow conditions. Furthermore, inertialess symmetry-breaking shape profiles at steady state are found as the bubble transits near the tipping points of the solution branches, which are shown both in experiments and numerical simulations.

This draft was prepared using the LaTeX style file belonging to the Journal of Fluid Mechanics 1

Non-unique bubble dynamics in a vertical capillary with an external flow

Yingxian Estella Yu[1], Mirco Magnini[2], Lailai Zhu[1,3], Suin Shim[1], and Howard A. Stone[1]†

[1]Department of Mechanical and Aerospace Engineering, Princeton University, Princeton, NJ 08544, USA

[2]Department of Mechanical, Materials and Manufacturing Engineering, University of Nottingham,
Nottingham, NG7 2RD, UK

[3]Department of Mechanical Engineering, National University of Singapore, 117575, Singapore

(Received xx; revised xx; accepted xx)

We study bubble motion in a vertical capillary tube under an external flow. Bretherton (1961) has shown that, without external flow, a bubble can spontaneously rise when the Bond number ($\mathrm{Bo} \equiv \rho g R^2/\gamma$) is above the critical value $\mathrm{Bo}_{cr} = 0.842$, where ρ is the liquid density, g the gravitational acceleration, R the tube radius, and γ the surface tension. It was then shown by Magnini *et al.* (2019) that the presence of an imposed liquid flow, in the same (upward) direction as buoyancy, accelerates the bubble and thickens the liquid film around it. In this work we carry out a systematic study of the bubble motion under a wide range of upward and downward external flows, focusing on the inertialess regime with Bond numbers above the critical value. We show that a rich variety of bubble dynamics occur when an external downward flow is applied, opposing the buoyancy-driven rise of the bubble. We reveal the existence of a critical capillary number of the external downward flow ($\mathrm{Ca}_l \equiv \mu U_l/\gamma$, where μ is the fluid viscosity and U_l is the mean liquid speed) at which the bubble arrests and changes its translational direction. Depending on the relative direction of gravity and the external flow, the thickness of the film separating the bubble surface and the tube inner wall follows two distinct solution branches. The results from theory, experiments and numerical simulations confirm the existence of the two solution branches and reveal that the two branches overlap over a finite range of Ca_l, thus suggesting non-unique, history-dependent solutions for the steady-state film thickness under the same external flow conditions. Furthermore, inertialess symmetry-breaking shape profiles at steady state are found as the bubble transits near the tipping points of the solution branches, which are shown both in experiments and three-dimensional numerical simulations.

Key words: thin films, lubrication theory, non-uniqueness, symmetry breaking

1. Introduction

The motion of an elongated bubble confined in a narrow geometry is of interest to a wide range of science and engineering fields, and can be found in various processes in industry, geology, and medical applications. Examples include oil production and

† Email address for correspondence: hastone@princeton.edu

recovery (e.g. Blunt 2001; Zhou & Prosperetti 2019), surface cleaning (e.g. Khodaparast *et al.* 2017; Asayesh *et al.* 2017), coating processes (e.g. Quéré 1999; Kotula & Anna 2012; Yu *et al.* 2017), medical therapy (e.g. Feinstein *et al.* 1984; Uhlendorf & Hoffmann 1994; Hu *et al.* 2015), heat exchange (e.g. Ferrari *et al.* 2018; Magnini & Matar 2020), etc. As a bubble translates in a liquid-filled capillary under an external flow, a thin film of liquid, separating the bubble surface and the inner tube wall, is formed owing to the competition of viscous and surface tension effects. It is of particular interest to understand the thickness of this lubricating film because it is responsible for the heat and mass transfer performance of the system. Furthermore, as in many of the applications mentioned above, the stability of the process and its efficiency are dependent on the thin film thickness and/or the interactions with the bubble surface. As a result, understanding the correlation between the film thickness and an applied external flow is the key to enable fine-tuning of the film thickness for better process control.

As first described theoretically by Bretherton (1961), for a horizontal configuration with negligible buoyancy effects, the lubricating film is uniform near the center body of the bubble, and the dynamics can be described by a single dimensionless number, the capillary number of the bubble $\mathrm{Ca}_b \equiv \mu U_b/\gamma$, where U_b is the bubble velocity, μ and γ represent the dynamic viscosity of the fluid and surface tension, respectively. In the limit of small bubble velocity, $\mathrm{Ca}_b < 5 \times 10^{-3}$, the uniform film thickness, b, relative to the inner radius of the cylindrical capillary, R, satisfies $b/R = 0.643\,(3\mathrm{Ca}_b)^{2/3}$. In the inertialess regime ($\mathrm{Re} \ll 1$, where $\mathrm{Re} \equiv \rho U_b R/\mu$ and ρ denotes the fluid density), this relationship was further extended to $\mathrm{Ca}_b < 2$ by Aussillous & Quéré (2000) as

$$\frac{b}{R} = \frac{1.34\mathrm{Ca}_b^{2/3}}{1 + 3.35\mathrm{Ca}_b^{2/3}}. \tag{1.1}$$

In both limits, the bubble velocity and the external flow velocity can be related by $\mathrm{Ca}_l/\mathrm{Ca}_b = (1 - b/R)^2$, where $\mathrm{Ca}_l \equiv \mu U_l/\gamma$, and U_l represents the cross-sectionally averaged external flow velocity.

In a system where buoyancy effects are not negligible, the Bond number $\mathrm{Bo} \equiv \rho g R^2/\gamma$ can be used to quantify the gravitational effects, with g denoting the acceleration of gravity. As described in the same paper characterizing the horizontal configuration, Bretherton (1961) predicted that the bubble will rise spontaneously in a vertically oriented capillary through a stagnant fluid for $\mathrm{Bo} > \mathrm{Bo}_{cr} = 0.842$. While Bo_{cr} has been confirmed by subsequent investigations (Lamstaes & Eggers 2017; Li *et al.* 2019; Dhaouadi & Kolinski 2019), the experimental film thickness measured by Thulasidas *et al.* (1995) shows deviation from Bretherton's prediction for a bubble rising under a small coflow. Thereafter, many studies in the literature have investigated the combined effects of buoyancy and external flow on the bubble motion, but the majority of the research has focused on the regime with $\mathrm{Bo} \gg 1$, where buoyancy and inertial effects dominate the dynamics (e.g. Nicklin 1962; Collins *et al.* 1978; Taitel *et al.* 1980; Polonsky *et al.* 1999; Araújo *et al.* 2012). Under these circumstances, the bubble always rises with a thick annular film, as well as a flattening, or even fragmented, bottom end. The steady thin films, relied on in many of the industrial and medical processes mentioned above, thus cannot be obtained in this inertia-dominant regime, but they can be achieved in the buoyancy-capillary dominant regime by reducing the Bond number.

Recently, Magnini *et al.* (2019) revisited the bubble dynamics in a vertical capillary under external flow for $\mathrm{Bo} \lesssim 1$. The authors showed that an upward external flow accelerates the rise of the bubble and thus thickens the film, and suggested that the same theoretical results could be applied to the case with a downward external flow;

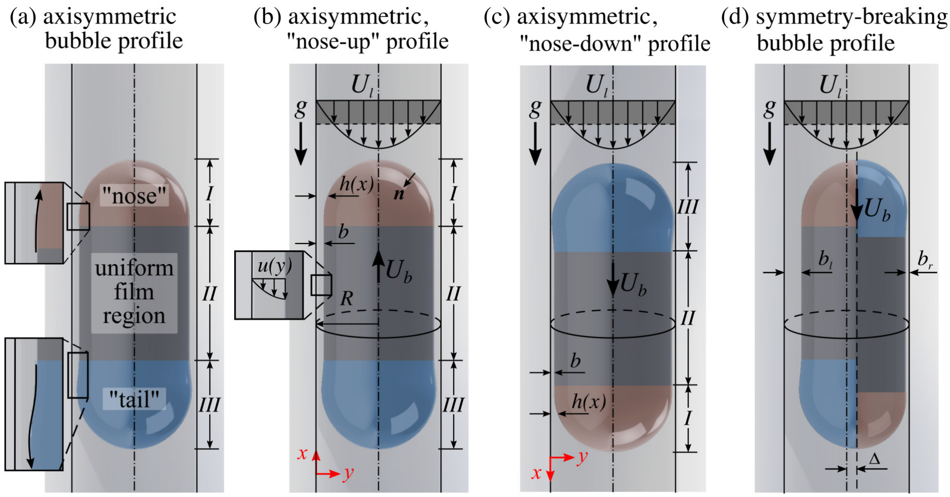

FIGURE 1. Schematics of bubble profiles. Bubbles are confined in a vertically oriented cylindrical capillary under an external flow, which is characterized by the cross-sectional averaged fluid velocity U_l, whose magnitude is shaded in dark gray. (a) Different regions in an axisymmetric bubble profile. The axisymmetric bubble profile is characterized by three distinct regions – I (shaded red): the bubble "nose", II: uniform film region, and III (shaded blue): the bubble "tail". As the arrows shown in the insets, when moving away from the uniform film region II, the film thickness connecting to the nose varies monotonically, while the film connecting to the bubble tail exhibits undulations. (b) Axisymmetric bubble profile with the nose pointing upward and the uniform film thickness $h(x) = b$ in region II. The inset shows a parabolic velocity profile $u(y)$ in region II in the lab frame. (c) Axisymmetric bubble profile with the nose pointing downward. Note that panels (b,c) are illustrated at the same magnitude of downward flow speed U_l, suggesting the non-unique film profiles under the same flow conditions. (d) The symmetry-breaking bubble profile, which shows the cross-section with the maximum (left) and minimum (right) film thicknesses. While the thick film adopts a profile with the nose (red) pointing upward and the tail (blue) pointing downward, the thin film profile has the opposite arrangement. The bubble centerline offsets from the tube centerline towards the thin film. The symmetry breaking will be discussed in §4.2.

the latter suggestion, however, lacked experimental confirmation. As we shall see in the current work, the external downward flow regime, in fact, contains richer dynamics than expected. Not only does the film profile admit different solution branches, but we find that multiple solutions are possible in some range of external downward flow, i.e. there is non-uniqueness. Thus, it is important to investigate the full picture of the correlation between the bubble profiles, buoyancy effects, and external flow, which shall provide further insights for enhancing the controllability of technologies involving thin films.

In this paper, we investigate the dynamics of a bubble in the inertialess regime at $\mathrm{Bo} \gtrsim \mathrm{Bo}_{cr}$, where the bubble is confined in a vertically oriented channel and translates at a steady state under a general external flow. By identifying the distinct bubble morphologies under different alignments between gravity and the external flow, we solve for the bubble profile combining efforts in theory, experiments and direct numerical simulations. Theoretical derivations are provided in §2, which provides the governing equations for determining the different solution branches of the film profile. Experiments and direct numerical simulations are both adopted for consolidating the theoretical predictions, with the methods described in §3. Results from theory, experiments and simulations are compared in §4. A phase diagram is then generated, providing a full picture of the axisymmetric bubble profiles and their uniform film thicknesses based on the combinations of Bo and Ca_l, including the direction of the external flow relative to gravity. Furthermore, inertialess symmetry-breaking bubble profiles are found in both experiments and simulations, with the characteristic features described in §4.2.

2. Theoretical derivation

The theoretical derivation in this section assumes azimuthal symmetry in the bubble profile (figure 1a-c). An axisymmetric bubble, for example in figure 1a, can be divided into three regions: a leading spherical cap (region I, also known as the "nose"), which smoothly connects to a uniform film region with thickness b (region II), and a trailing spherical cap (region III, also known as the "tail"), which connects to region II with undulations. For a bubble in a vertically oriented capillary under an external flow, two possible axisymmetric bubble profiles can be obtained, including the "nose-up" (figure 1b) and the "nose-down" (figure 1c) configurations. In this section, theoretical derivations will be provided to solve for the uniform film thickness in these two cases.

As mentioned previously, the classic Bretherton problem in a horizontal capillary can be considered as the special case with $\mathrm{Bo} = 0$. In the absence of buoyancy effects, the tube orientation does not alter the dynamics, and the uniform film thickness is solely determined by the magnitude of the external flow. The film thickness vanishes as $\mathrm{Ca}_l \to 0$, with the direction of the bubble motion and the bubble nose pointing in the same direction as the external flow.

In the case where Bo is not negligible, the dynamics of the bubble are governed by the combination of viscous and capillary effects, buoyancy, and the external flow. Since a bubble can spontaneously rise through a stagnant fluid in a vertically oriented capillary when $\mathrm{Bo} > \mathrm{Bo}_{cr}$, it is intuitive that this bubble might sustain a small magnitude of the downward flow and continue to rise. As will be shown later in this section, the directional alignment between the two driving forces will significantly affect the axisymmetric bubble profile, which can be categorized naturally in one of two cases: a bubble with the "nose" pointing upward or downward. In this problem, the Bond number $\mathrm{Bo} = \rho g R^2/\gamma$ and the capillary number of the external flow $\mathrm{Ca}_l = \mu U_l/\gamma$ are both given. Based on the input, we seek to uncover the dynamics of the bubble at steady state, especially the uniform film thickness b/R as well as the nondimensional speed, or the capillary number of the bubble, $\mathrm{Ca}_b = \mu U_b/\gamma$. Hereafter, negative values of the liquid or bubble capillary number are associated with downward liquid or bubble flow.

2.1. *"Nose-up" branch: bubble profile with nose pointing upward*

We begin by summarizing the results from Magnini *et al.* (2019), who investigated the dynamics of a confined bubble translating at steady state under an external upward flow. In fact, with a small variation, as we will describe in the following context, it can be extended to describe a more general case: the dynamics of a bubble with its "nose" pointing upward (figure 1b).

As indicated in figure 1b, the coordinates are represented by (x, y), with x pointing vertically upward, and $y = R - r$ pointing radially inward from the tube inner wall. With the assumption that the film thickness is much smaller than the tube radius, $b/R \ll 1$, (x, y) can effectively be treated as the local Cartesian coordinates, and the lubrication approximation can be applied to simplify the Navier-Stokes equations as

$$\text{continuity:} \qquad u_x + v_y = 0, \tag{2.1a}$$

$$x \text{ direction:} \qquad u_{yy} = \frac{1}{\mu}\left(p_x + \rho g\right), \tag{2.1b}$$

$$y \text{ direction:} \qquad p_y = 0, \tag{2.1c}$$

where subscripts denote derivatives, the velocities in (x, y) are represented by (u, v), and p denotes the fluid pressure.

In a reference frame moving with the bubble at the steady-state speed U_b, the velocity profile within the thin film can be obtained by integrating equation (2.1b) with the boundary conditions

$$u\big|_{y=0} = -U_b \quad \text{and} \quad u_y\big|_{y=h(x)} = 0, \tag{2.2}$$

which results in

$$u(y) = \frac{1}{2\mu}\left(p_x + \rho g\right)\left(y^2 - 2hy\right) - U_b. \tag{2.3}$$

Note that due to the gravitational effects, fluid in the thin film is always draining vertically downward with a parabolic profile. Specifically, the velocity profile within the uniform film region $u_b(y) = \rho g(y^2 - 2by)/(2\mu) - U_b$ can then be obtained by demanding $h(x) = b$ and $p_x = 0$ from equation (2.3). An expression for κ_x, the gradient of curvature along the $x-$direction, can thus be obtained by matching the fluxes from integrating the two velocity profiles, and, consistent with the relative magnitude of terms in the lubrication approximation, expressing the gradient of capillary pressure as $p_x = -\gamma\kappa_x$:

$$\kappa_x = \frac{3\mu U_b}{\gamma}\frac{(h-b)}{h^3} + \frac{\rho g}{\gamma}\frac{\left(h^3 - b^3\right)}{h^3}. \tag{2.4}$$

The two terms in (2.4) indicate the contributions from the capillary and buoyancy effects, respectively. This expression for κ_x, obtained from the lubrication equations, can be equated to its geometrical counterpart, $\kappa_x = (\nabla \cdot \mathbf{n})_x$, where $\mathbf{n}$ denotes the normal vector of the bubble surface pointing inward to the gas phase (figure 1b), leading to

$$\frac{3\mu U_b}{\gamma}\frac{(h-b)}{h^3} + \frac{\rho g}{\gamma}\frac{\left(h^3 - b^3\right)}{h^3} = \left[\frac{1}{(h_x^2+1)^{1/2}}\frac{1}{R-h} + \frac{h_{xx}}{(h_x^2+1)^{3/2}}\right]_x. \tag{2.5}$$

As noticed previously (Magnini *et al.* 2019), the full expression for the curvature of the film profile is necessary in order for equation (2.4) to describe the liquid flow both in the thin film and the bubble caps regions. One can further proceed with nondimensionalization by defining $X = x/\ell$, $H = h/b$, and $K = \kappa\ell^2/b$, with ℓ denoting the characteristic length scale in the $x-$direction, which will be determined below. Different from Magnini *et al.* (2019), nondimensionalizing equation (2.5) shows that there are two choices for the characteristic scale ℓ, which lead to two different expressions for $\epsilon \equiv b/\ell$:

$$\epsilon_1 = \mathrm{Ca}_b^{1/3} \quad \text{or} \quad \epsilon_2 = \left(\alpha^2 \mathrm{Bo}\right)^{1/3}, \tag{2.6}$$

where $\alpha = b/R$. Note that ϵ_1 and ϵ_2 are consistent with the characteristic scales for the classic Bretherton problems in horizontal ($\mathrm{Bo} = 0$) and vertical orientations ($\mathrm{Ca}_l = 0$), respectively. Furthermore, the ratio between these two choices, $\lambda \equiv (\epsilon_2/\epsilon_1)^3 = \alpha^2\mathrm{Bo}/\mathrm{Ca}_b$, quantifies the relative significance of the buoyancy and capillary effects within the thin

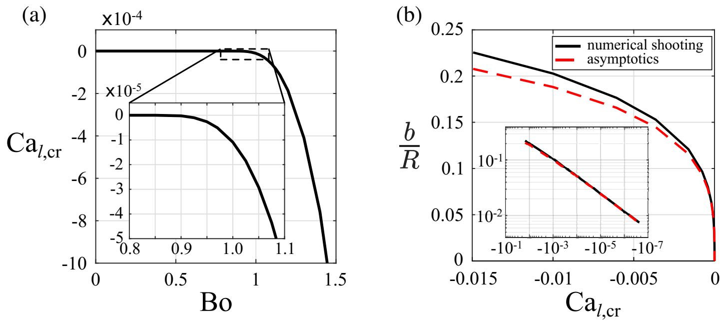

FIGURE 2. Critical condition for a bubble being stabilized in the lab frame ($\mathrm{Ca}_b = 0$) under an external downward flow. (a) The critical strength of the external flow $\mathrm{Ca}_{l,cr}$ as a function of Bo. Consistent with results in the literature, external downward flow is needed for keeping the bubble stationary in the lab only for $\mathrm{Bo} > \mathrm{Bo}_{cr}$, and as Bo increases, a stronger downward flow is required. (b) The uniform film thickness b/R when the critical external flow condition $\mathrm{Ca}_{l,cr}$ is applied, where $\alpha = b/R$ monotonically increases with $\mathrm{Ca}_{l,cr}$. In the limit of $\alpha \to 0$, expanding equation (2.9) shows that $\alpha \sim (-\mathrm{Ca}_{l,cr}/\mathrm{Bo})^{1/3}$, and the asymptotic scaling is shown as the red dashed curves.

film region. While the right-hand side (RHS) of the rescaled (2.5) shows

$$\mathrm{RHS} = \frac{H_{XXX}}{f^3} - \frac{3\epsilon^2 H_X H_{XX}^2}{f^5} - \frac{\alpha}{1-\alpha H}\frac{H_X H_{XX}}{f^3} + \left(\frac{\alpha}{1-\alpha H}\right)^2 \frac{H_X}{\epsilon^2 f}, \tag{2.7}$$

with $f = \left(\epsilon^2 H_X^2 + 1\right)^{1/2}$, different choices of ϵ result in a slightly different left-hand side (LHS) of the rescaled (2.5):

$$\epsilon = \epsilon_1 : \quad \mathrm{LHS} = 3\frac{(H-1)}{H^3} + \lambda\frac{(H^3-1)}{H^3} \tag{2.8a}$$

$$\text{or} \quad \epsilon = \epsilon_2 : \quad \mathrm{LHS} = \frac{3}{\lambda}\frac{(H-1)}{H^3} + \frac{(H^3-1)}{H^3}. \tag{2.8b}$$

When the system is provided with an upward external flow, as in Magnini *et al.* (2019), both length scale choices are well defined and thus perform equivalently. When solving for the film profile with a downward flow, however, choosing ϵ_1 becomes problematic as $\mathrm{Ca}_b \to 0$, which leads to an artificial singularity in the term associated with λ in (2.8*a*).

As a result, in order to extend the film profile solution with an upward nose towards the downward flow regime, while avoiding the artificial singularity, the characteristic length scale is chosen interactively during the numerical shooting process (see §2.3 for more detail): $\epsilon = \epsilon_1$ is chosen when $\lambda < 1$, where capillary effects outweigh buoyancy in the thin film and equations (2.7, 2.8*a*) are solved; otherwise, when $\lambda \geqslant 1$, $\epsilon = \epsilon_2$ is chosen and equations (2.7, 2.8*b*) are solved.

Note that in the simulations and physical experiments, the strength of the external flow, Ca_l, is directly controlled rather than the bubble speed, Ca_b, which enters $\lambda = \alpha^2\mathrm{Bo}/\mathrm{Ca}_b$. Therefore, an additional relationship is needed to link the two capillary numbers, which can be obtained by balancing the flux from the external Poiseuille flow in the far field and the cross-sectional flux in the uniform film region. Integrating the velocity profiles in cylindrical coordinates, we have

$$\mathrm{Ca}_b = \frac{\mathrm{Ca}_l}{(1-\alpha)^2} + \mathrm{Bo}\left[-\frac{1}{2} + \frac{3(1-\alpha)^2}{8} + \frac{1}{8(1-\alpha)^2} - \frac{1}{2}(1-\alpha)^2\log(1-\alpha)\right]. \tag{2.9}$$

With any two of Bo, Ca_l, Ca_b, and $\alpha = b/R$ given, one can solve equations (2.7, 2.8, 2.9) for the other quantities with numerical shooting (see §2.3). One of the questions of interest is the critical strength of the external downward flow needed, $\mathrm{Ca}_{l,cr}$, in order to stabilize the bubble, i.e., $\mathrm{Ca}_b = 0$. In this scenario, the critical magnitude of external flow $\mathrm{Ca}_{l,cr}$ and the corresponding film thickness $\alpha = b/R$ can be solved based on the two inputs – the Bond number Bo and $\mathrm{Ca}_b = 0$.

Typical results from a numerical solution are shown in figure 2, where the critical downward flow $\mathrm{Ca}_{l,cr}$ as a function of Bo is shown as the black solid curve in panel (a). For a fixed Bo, the bubble rises if the provided external flow is above the curve with $\mathrm{Ca}_l > \mathrm{Ca}_{l,cr}$, and vice versa. This solution is consistent with the results for a vertically oriented capillary in Bretherton (1961), as $\mathrm{Ca}_{l,cr} = 0$ remains true for all $\mathrm{Bo} < \mathrm{Bo}_{cr}$, and nonzero downward flow is needed to maintain the bubble stationary in the lab frame otherwise. The magnitude of $\mathrm{Ca}_{l,cr}$ remains small for $\mathrm{Bo} \approx 1$, and rapidly increases as gravitational effects become more dominant.

The corresponding critical film thickness is shown in figure 2b, where the inset is plotted in log-log scales. Note that in the limit of $\alpha \to 0$, equation (2.9) can be expanded. Since both the external flow and buoyancy are significant, taking the leading order of each term and demanding $\mathrm{Ca}_b = 0$ (a stationary bubble) leads to

$$\alpha = \left(-\frac{3}{2}\frac{\mathrm{Ca}_{l,cr}}{\mathrm{Bo}}\right)^{1/3}. \tag{2.10}$$

This asymptotic approximation is shown in figure 2b as the red dashed curve, which is in excellent agreement with the numerical shooting solutions for $\alpha = b/R < 0.1$. Furthermore, the rapid increase of $\mathrm{Ca}_{l,cr}$ with Bo can thus be qualitatively explained, since the critical film thickness increases with Bo, and the scaling shows $|\mathrm{Ca}_{l,cr}| \sim \alpha^3 \mathrm{Bo}$.

2.2. *"Nose-down" branch: bubble with nose pointing downward*

Equations (2.7, 2.8, 2.9) fully describe the dynamics of the bubble under an upward external flow ($\mathrm{Ca}_l \geqslant 0$). For $\mathrm{Bo} > \mathrm{Bo}_{cr}$, the solution can be further extended towards the downward flow regime ($\mathrm{Ca}_l < 0$), with the bubble nose pointing upward and $\mathrm{Ca}_b \to \mathrm{Ca}_l^+$. However, this solution is only valid for a limited range of $\mathrm{Ca}_l < 0$, beyond which solutions of equations (2.7, 2.8, 2.9) fails to converge within the set tolerance, and thus the branch terminates. In a physical system, the bubble responds to the stronger downward flow by changing its morphology, so that the "nose" points downward as indicated in figure 1c, following the flow direction. Both experiments and simulations introduced in the next sections will confirm this response.

The bubble profile in a downward-nose system is similar to the upward-nose case, and therefore when it comes to solving for the film profile, the new film equations can be obtained by modifying equations (2.7, 2.8, 2.9) simply by redefining the vertical coordinate as $\tilde{x} = -x$ (figure 1c). With this convention, the positive directions of Ca_l and Ca_b within the model are redefined, while the scalar variables (e.g. α and H) remain unchanged. Furthermore, since the gravitational direction remains vertically downward regardless of coordinates, in the new coordinate system, the terms associated with Bo must change sign as well. As a result, the film equations become

$$3\frac{(H-1)}{H^3}-\lambda\frac{(H^3-1)}{H^3} = \frac{H_{XXX}}{f^3}-\frac{3\epsilon^2 H_X H_{XX}^2}{f^5}-\frac{\alpha}{1-\alpha H}\frac{H_X H_{XX}}{f^3}+\left(\frac{\alpha}{1-\alpha H}\right)^2\frac{H_X}{\epsilon^2 f}, \tag{2.11a}$$

$$\mathrm{Ca}_b=\frac{\mathrm{Ca}_l}{(1-\alpha)^2}-\mathrm{Bo}\left[-\frac{1}{2}+\frac{3\,(1-\alpha)^2}{8}+\frac{1}{8\,(1-\alpha)^2}-\frac{1}{2}\,(1-\alpha)^2\log(1-\alpha)\right], \tag{2.11b}$$

where, compared to equations (2.7, 2.8, 2.9), the net effects are sign changes in the terms related to gravity only. In other words, by changing the nose direction from upward to downward, the bubble only senses a sign change in the buoyancy force: instead of assisting the bubble to rise, buoyancy effects are now acting as resistance to the bubble motion, which is now mainly driven by the downward external flow.

When the bubble dynamics falls on this solution branch, the bubble always sinks and the film thickness α converges to the origin as $\mathrm{Ca}_l \to 0^-$ (as we will confirm in §4). Thus, $\epsilon = \epsilon_1$ is chosen when nondimensionalizing the equations, resulting in the form of (2.11*a*) similar to (2.8*a*).

2.3. *Numerical integration*

With Ca_l and Bo given, equations (2.7, 2.8, 2.9) or (2.11) can be solved for Ca_b, the uniform film thickness α and the film profile $H(X)$, with the boundary conditions

$$H(0)=1, \quad H_X(0)=0, \quad \text{and} \quad H_{XX}(0)=0, \tag{2.12}$$

and $H(X_{nose}) = 1/\alpha$ is demanded as the additional constraint, with $X = 0$ indicating the uniform film region and X_{nose} the location of the bubble nose, which is yet to be determined by the numerical integration scheme. Although the full curvature of the film is used in equations (2.7, 2.8, 2.9) or (2.11), the underlying solution method is effectively the same as the asymptotic expansion as seen in Bretherton (1961), which includes the process of solving the film equation for the bubble "nose" and matching to the static spherical cap. The coupled equations are solved by first imposing an initial guess on α. With Ca_l and Bo given, equation (2.9) or (2.11*b*) outputs the capillary number of the bubble Ca_b, which serves as an input for equation (2.7, 2.8) or (2.11*a*). The ODE for $H(X)$ is solved by numerical integration with Matlab *ode*45 from the uniform film region towards the front spherical cap in the positive X-direction. Numerical integration ceases when $H_X \to \infty$, where the termination location denotes X_{nose} and the value $H(X_{nose})$ is compared with the constraint $H(X_{nose}) = 1/\alpha$. The initial guess of α is then iteratively updated until this additional constraint is met, meaning that the bubble nose is symmetric about the tube centerline.

3. Experimental and numerical simulation methods

3.1. *Experimental setup*

Experiments are performed in a refractive index matching setup similar to those described in Yu *et al.* (2018) and Magnini *et al.* (2019), with pure glycerol filling the capillary tube as the continuous phase. Density, viscosity and surface tension of the pure glycerol are measured as $\rho = (1.29 \pm 0.001) \times 10^3$ kg m^{-3}, $\mu = 1.00 \pm 0.04$ Pa s (Anton Parr, Physica MCG 301), and $\gamma = 65.4 \pm 1.0$ mN m^{-1} (pendant drop), respectively.

Glass capillaries with three different inner diameters ($ID = 4.45, 4.85, 5.65 \pm 0.05$ mm) are used, yielding the Bond numbers of Bo $= 0.97, 1.16, 1.56$, respectively. Each glass capillary is placed within in a cuboid glassed box, which is also filled with pure glycerol in order to avoid imaging distortions. The top end of the glass capillary is connected to a liquid reservoir by a Teflon hose, and the bottom end is submerged in a bath of pure glycerol. The experimental flow rate is adjusted by controlling the reservoir pressure using the Elveflow® OB1 MK3 pressure and vacuum controller, and calibration between the flow rate and controller pressure is performed for all capillary tubes used. The imaging apparatus is composed of a Nikon D5100 DSLR camera and a Mitutoyo infinity corrected objective, mounted on a house-made tube microscope. The imaging apparatus is aligned horizontally with a collimated LED light source, which is located half way between the two ends of the capillary tube.

In each set of experiments with the same Bo, the capillary tube is partially filled with pure glycerol, leaving a section of an air column in the bottom end of the capillary. The setup is then carefully calibrated to be vertical. A single bubble is formed by applying vacuum to the system, providing an upward flow and assisting the formation of the thin liquid film. For experiments corresponding to $\mathrm{Ca}_b > 0$, experiments start by directly setting the pressure/vacuum to a target value; for experiments with $\mathrm{Ca}_b < 0$, on the other hand, the target pressure value is set after the bubble rises to the top end of the capillary. As the bubble reaches the region of interest of the imaging apparatus, the dynamics of the bubble are recorded in the bright-field mode at 30 fps. After each experiment, the bubble velocity and the film profile are analyzed from the image sequence, and the capillary number of the external flow Ca_l is calculated based on the calibration between flow rate and pressure control.

3.2. *Numerical simulation setup*

Direct numerical simulations of the flow of elongated bubbles in vertical capillaries are performed utilising the Volume-of-Fluid (VOF) method (Hirt & Nichols 1981) implemented in OpenFOAM. The unsteady mass and momentum equations for an incompressible flow and Newtonian fluid are solved, together with a transport equation for a passive scalar that identifies the gas and liquid phases across the domain. In this formulation, the surface tension force is implemented as a body force according to the Continuum Surface Force method (Brackbill *et al.* 1992). Both two-dimensional axisymmetric and full three-dimensional simulations are conducted, with the latter enabling us to investigate conditions that may lead to symmetry breaking. The simulation setup is similar to that adopted in previous works (Magnini *et al.* 2019, 2017). An elongated bubble, with the shape of a cylinder with spherical ends, is initialized at one end of the flow domain. Bubble lengths of about $6D$ are sufficient to achieve a uniform film region between front and rear menisci, under the conditions of interest. At the inlet boundary, a fully developed laminar profile is set for the incoming liquid, while no-slip is set at the pipe wall. At the channel outlet, pressure is given a constant value, together with a zero gradient condition for the velocity. The liquid to gas density and viscosity ratios are set to 1000 and 100, respectively. Each simulation is run forward in time until the bubble translates with a constant speed.

Numerical simulations are performed for the three values of the Bond number tested experimentally and a wide range of Ca_l, for both upward and downward liquid flow. For each value of Bo and each flow direction, a first simulation is run with the largest $|\mathrm{Ca}_l|$ desired, until steady state. From this steady solution, $|\mathrm{Ca}_l|$ is reduced and a new simulation is run until a new steady bubble profile and speed are achieved. The procedure

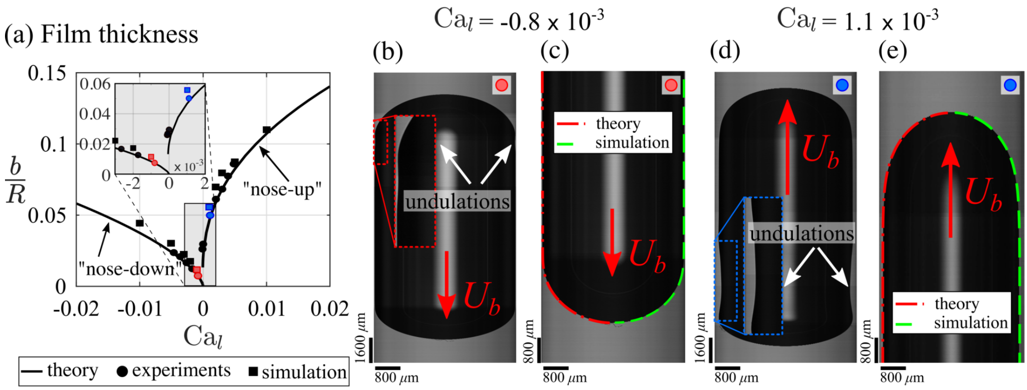

FIGURE 3. Comparison between lubrication theory, experiments, and simulations at $\mathrm{Bo} = 0.97$. (a) b/R versus Ca_l. Solid curves represent the theoretical results from numerical shooting, with the "nose-down" branch obtained from solving (2.11), and the "nose-up" branch from solving (2.7, 2.8, 2.9). Results from experiments (circles) and direct numerical simulations (squares) both agree with the theoretical prediction and verify the existence of two distinct branches. Specifically, the red and blue markers represent the cases shown in (b,c) and (d,e), respectively. (b,c) Bubble with nose pointing downward, where undulations appear on the top end of the bubble. Bubble profiles are compared in (c), where the theoretical profile (red dash-dotted curve) is plotted on the left, and the profile from numerical simulation (green dashed curve) is plotted on the right. (d,e) Bubble with nose pointing upward with undulations appearing on the bottom end. Results are compared in (e) with the theoretical profile (red dash-dotted curve) on the left, and the simulation profile (green dashed curve) on the right.

continues by stepping towards smaller values of $|\mathrm{Ca}_l|$ to span the entire range of conditions of interest, each time until steady state.

4. Results and discussion

The comparison between theory, experiments and numerical simulations is shown in figure 3 for $\mathrm{Bo} = 0.97$. The film thickness b/R as a function of Ca_l is plotted in figure 3a, where results from theory (solid curves), experiments (circles), and numerical simulations (squares) show good agreement. The theoretical results from numerical shooting predict two distinct solution branches of the film thickness – the "nose-down" branch is obtained by solving (2.11), where the bubble nose is pointing downward; the "nose-up" branch is obtained from solving (2.7, 2.8, 2.9), with the bubble nose pointing upward. Note that since the Bond number $\mathrm{Bo} = 0.97 > \mathrm{Bo}_{cr}$, the "nose-up" branch intersects with the y-axis (stagnant fluid) at a non-zero value of the film thickness. As Ca_l decreases towards the downward flow regime, the "nose-up" branch extends towards $b/R \to 0$, but only exists in a very narrow range of downward flow before it terminates; this aspect will be more apparent at the larger Bond numbers presented in the next section.

As displayed in figure 3, under the same magnitude of the external flow, the film thickness on the "nose-up" branch is consistently larger than that on the "nose-down" branch. As an example, typical experimental images are shown for a sinking bubble (figure 3b,c, corresponding to the red markers in figure 3a), and a rising bubble (figure 3d,e, corresponding to the blue markers in figure 3a). While the sinking bubble shown in the figure has its nose pointing downward and undulations appear near the top end, the rising bubble has its nose pointing upward and undulations appear near the bottom end. For the two cases undergoing an external flow of similar magnitude, the sinking bubble (figure 3c) shows a film thickness of $b/R = 7.6 \times 10^{-3}$, which is much smaller than that of a rising bubble (figure 3e), whose film thickness is $b/R = 5.0 \times 10^{-2}$. Furthermore, the film profiles near the bubble nose are also compared. As shown in figure 3c,e, the theoretical film profiles are plotted as red dash-dotted curves, overlaying on the left half of the experimental images, and the profiles from simulations are plotted as green dashed lines on the right. In both cases, good agreement is obtained among the theoretical, experimental, and numerical results.

4.1. *Effects of Bo and the non-unique, history-dependent film profiles*

Results for different Bond numbers $\text{Bo} = \{0.97, 1.16, 1.56\}$ are displayed in figure 4. Note that only the results of experiments and simulations terminating with an axisymmetric bubble profile are included in the figure, whereas symmetry-breaking configurations will be discussed in §4.2. As the Bond number increases in figure 4a,c,e, the film thickness on the two branches deviate more from the classic theory (equation (1.1), shown as gray dashed curves), and the difference between the two branches also increases. As the film thickness on the "nose-up" branch increases along with Bo, the branch intersects with the y-axis at a larger value of b/R. The "nose-down" branch, however, has the film thinning as Bo increases, which is consistent with the physical intuition. When the bubble translates with an upward nose, buoyancy serves as the main driving force of the motion, and the external flow acts as a side factor, assisting or hindering the bubble motion depending on the sign of Ca_l. As a result, the bubble has an increased tendency to rise as Bo increases, and thus forms a thicker film. On the other hand, the external flow serves as the main driving force when the bubble sinks with a downward nose, while gravity remains a resistance to the bubble motion, thus resulting in the thinning of the film thickness at higher Bo. Meanwhile, comparing Ca_b and Ca_l at various Bo (figure 4b,d,f) shows that the bubbles with downward noses always sink with $\text{Ca}_b < \text{Ca}_l$. On the other hand, the bubbles on the "nose-up" branch follow $\text{Ca}_b > \text{Ca}_l$ over a wide range of Ca_l, except for a very narrow region near the branch termination (see insets of figure 4b,d,f).

Furthermore, we observe from both the film thickness and bubble capillary number plots that the "nose-up" branch extends towards the downward flow regime, with the extended domain enlarging for increasing values of the Bond number, whereas the "nose-down" branch always converges to the origin as $\text{Ca}_l \to 0^-$. These results suggest that there is a range of downward flows where the two branches overlap for the same Bo and Ca_l, and hence the bubble film profile undergoes "hysteresis"-like history-dependent dynamics in the overlapping domain of the two branches.

As an example, the inset of figure 4f shows the simulation results of two different film profiles obtained under the same conditions of $\text{Bo} = 1.56$ and $\text{Ca}_l = -2 \times 10^{-3}$. When the bubble profile is obtained starting from a steady-state configuration at $\text{Ca}_l = 0$, the solution stays on the "nose-up" branch (blue squares), which corresponds to a bubble sinking at $\text{Ca}_b = -7.5 \times 10^{-4}$ ($\text{Ca}_b > \text{Ca}_l$) with a thick film of thickness $b/R = 1.2 \times 10^{-1}$ and its nose pointing upward. However, a distinct solution is obtained when reaching $\text{Ca}_l = -2 \times 10^{-3}$ from a steady-state profile at a smaller (more negative) Ca_l, which belongs to the "nose-down" branch. The solution stays on the "nose-down" branch (red squares), and the bubble sinks at $\text{Ca}_b = -2.1 \times 10^{-3}$ ($\text{Ca}_b < \text{Ca}_l$) with a much thinner film of thickness $b/R = 1.5 \times 10^{-2}$ and its nose pointing downward.

To summarize the evolution of the two branches at different Bo, a phase diagram for the axisymmetric bubble profile is generated from the theoretical results and shown in figure 5. The classic theoretical results with $\text{Bo} = 0$ are plotted as the black solid curves, which are symmetric about the y-axis. When an external upward flow is applied, the bubble profile is uniquely determined by the combination of Bo and $\text{Ca}_l > 0$, and for

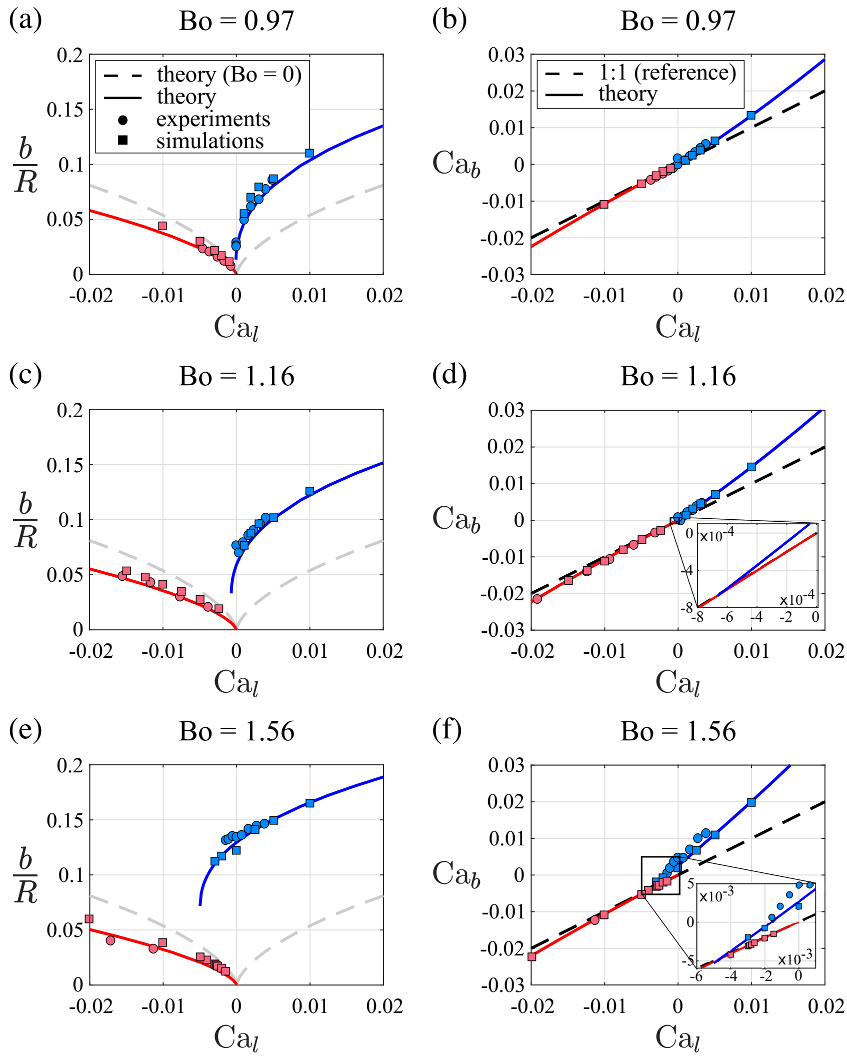

FIGURE 4. Overlapping solution branches and the non-unique film profiles for $\mathrm{Bo} > \mathrm{Bo}_{cr}$. Results at $\mathrm{Bo} = \{0.97, 1.16, 1.56\}$ are shown comparing theory (solid curves), experiments (circles) and numerical simulations (squares), where results corresponding to the "nose-down" branch (thin film) and "nose-up" branch (thick film) are colored in red and blue, respectively. The relationships between the film thickness b/R and external flow Ca_l are shown in panels (a), (c), (e). As Bo increases, the two solution branches deviate more from the classic $\mathrm{Bo} = 0$ theory (gray dashed curves) and overlap over a larger region of downward flow. The comparisons between Ca_b and Ca_l are shown in panels (b), (d), (f), with the black dashed line indicating the reference $\mathrm{Ca}_b = \mathrm{Ca}_l$. While $\mathrm{Ca}_b < \mathrm{Ca}_l$ is observed on the "nose-down" branch, the "nose-up" branch mainly follows $\mathrm{Ca}_b > \mathrm{Ca}_l$, except at a very narrow region close to where the branch terminates. The insets show a close-up view of the overlapping regions of the branches, where the history-dependent bubble dynamics are observed both theoretically and numerically.

the same Ca_l, the film thickness increases with Bo. Note that for $\mathrm{Bo} < \mathrm{Bo}_{cr}$, the film thickness converges to the origin as $\mathrm{Ca}_l \to 0^+$, which is consistent with the original work of Bretherton (1961). For $\mathrm{Bo} > \mathrm{Bo}_{cr}$, on the other hand, the "nose-up" branch extends into a limited range of downward flow speeds. The bubble continues to rise until the "nose-up" branch intersects with the black dash-dotted curve denoting $\mathrm{Ca}_b = 0$, and this

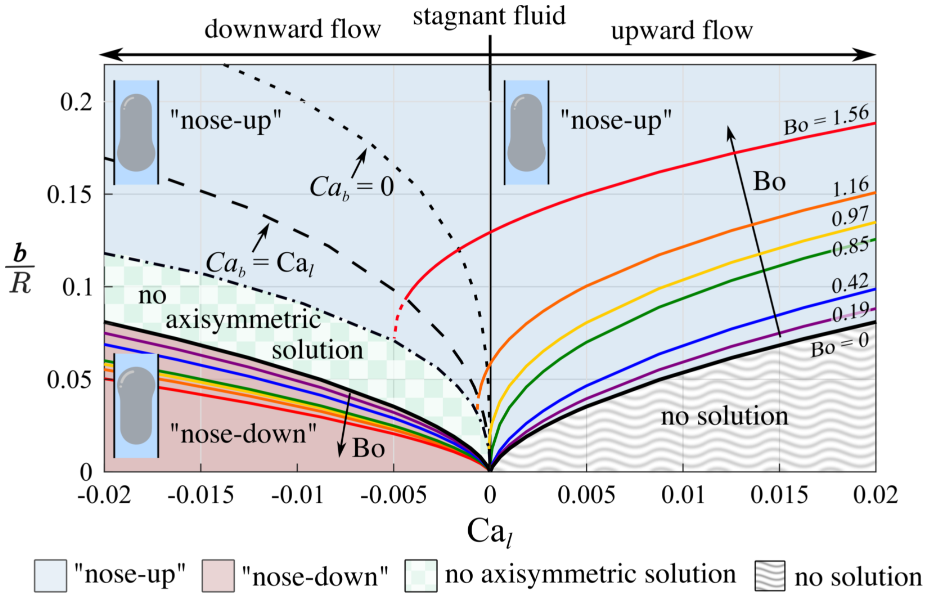

FIGURE 5. Phase diagram obtained from numerically integrating equations (2.7, 2.8, 2.9) and equation (2.11), showing the film thickness b/R versus Ca_l and the evolution of the branches with varying Bo. The two branches corresponding to the same Bo are labeled with the same color code. Also shown in each regime are schematics of the typical bubble profile. While the "nose-up" branches with $\mathrm{Bo} < \mathrm{Bo}_{cr}$ converge to the origin, the "nose-up" branches with $\mathrm{Bo} > \mathrm{Bo}_{cr}$ extend in the downward flow regime. The black dotted curve "- - - -" and black dashed curve "— —" represent the critical conditions where $\mathrm{Ca}_b = 0$ and $\mathrm{Ca}_b = \mathrm{Ca}_l$, respectively. The black dash-dotted curve "— · —" shows the conditions where the "nose-up" branches terminate in the numerical shooting schemes. Note that the "nose-up" branches are shown as dashed between $\mathrm{Ca}_b = \mathrm{Ca}_l$ and the branch termination conditions, since no axisymmetric bubble profiles are observed in experiments or 3D numerical simulations within this range, as will be explained in §4.2.

axisymmetric solution branch eventually terminates at the black dashed curve, beyond which the numerical shooting method fails to converge within the set tolerance when equations (2.7, 2.8, 2.9) are solved.

If Ca_l is further decreased beyond the region where the "nose-up" branch terminates, axisymmetric solutions can only be found on the "nose-down" branch with the bubble nose pointing downward, as shown in figure 5 with the color code being the same as the corresponding "nose-up" branch. With the external flow serving as the main driving force, for the same value of Ca_l, the bubble film thickness on the "nose-down" branch decreases with the increasing resistance from Bo. Since all solutions on the "nose-down" branches converge to the origin as $\mathrm{Ca}_l \to 0^-$, the solution branches overlap in the region where the "nose-up" branch extends in the downward flow regime, and the overlap region enlarges with increasing Bo, indicating the non-unique and history-dependent film thickness solutions.

4.2. *Symmetry breaking*

Numerical shooting results indicate that axisymmetric bubble profiles are not available in the downward flow region between the black solid curve (the "nose-down" branch with $\mathrm{Bo} = 0$) and the black dash-dotted curve (where the "nose-up" branches terminate), where both experiments and three-dimensional simulations exhibit symmetry-breaking

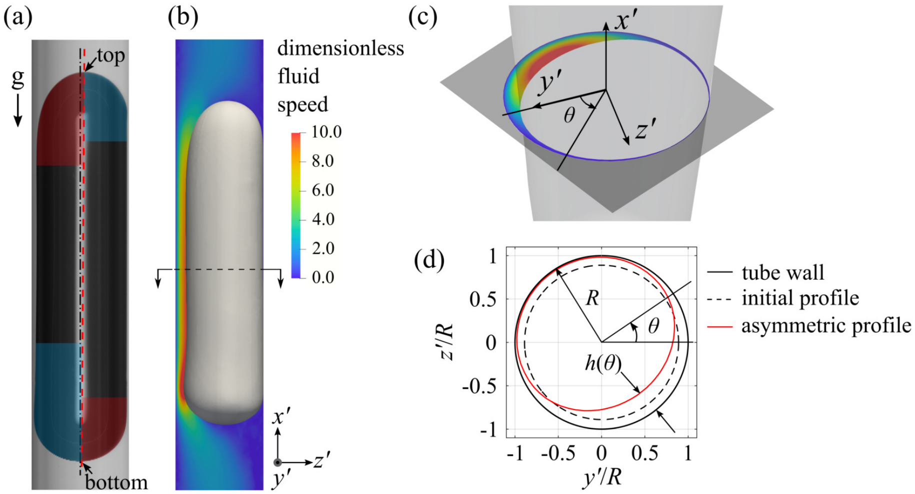

FIGURE 6. Symmetry-breaking bubble profiles in experiments and simulations. (a) Symmetry-breaking profiles obtained from experiments, with $\mathrm{Bo} = 0.97$, and $\mathrm{Ca}_l = -1.7\times10^{-3}$. Note that the "nose" (shaded red) and "tail" (shaded blue) of the bubble are the sections connecting to the uniform film region without and with undulations, respectively. A thick film is shown on the left-hand side with the bubble nose pointing upward, and a thin film is shown on the right-hand side with the bubble nose pointing downward. From the tube centerline (black dash-dotted line), the bubble centerline (red dashed line) is shifted towards the side of the thin film. (b-d) Symmetry-breaking profiles obtained from a 3D numerical simulation at $\mathrm{Bo} = 1.56$ and $\mathrm{Ca}_l = -4.0\times10^{-3}$, started from a steady-state configuration ($\mathrm{Ca}_l = -3.0\times10^{-3}$) belonging to the "nose-up" branch. (b) The symmetry-breaking profiles are consistent with the image obtained from experiments, with the color code representing the downward fluid velocity normalized by U_l. (c) The circumferential bubble profile about half way between the bubble top and bottom (as indicated by the dashed line in panel (b)), where the cross section of the bubble is no longer circular. (d) The bubble profile in the $y' - z'$ plane. The black solid circle represents the tube inner wall, and the black dashed circle and the red curve represent the initial axisymmetric bubble profile and the asymmetric bubble surface, respectively.

profiles, as it will be shown below; see sketch in 1d. Note that axisymmetry-breaking bubble profiles are known in the literature for pipe flows with $\mathrm{Bo} \geqslant \mathcal{O}(10)$, where the bubble breaks symmetry in external flows with large inertial effects ($\mathrm{Re} \gtrsim \mathcal{O}(100)$), often with fragmented bottoms (see e.g. Griffith & Wallis 1961; Martin 1976; Lu & Prosperetti 2006; Fabre & Figueroa-Espinoza 2014; Fershtman *et al.* 2017). In contrast, the symmetry-breaking profiles obtained in the current work, as shown in figure 6a,b, exist in an inertialess regime with $\mathrm{Bo} \leqslant \mathcal{O}(1)$ and $|\mathrm{Ca}_l| \leqslant \mathcal{O}(10^{-2})$. The bubble profile thus preserves some features associated with the classic lubricating film in an axisymmetric bubble.

Both experiments and 3D simulations yield symmetry-breaking profiles when the bubble attempts to transit between steady states near the ends of the two branches, while the bubble is sinking and adapting to a new steady-state profile by thinning the film. While the symmetry breaking profiles are supported by both experiments and 3D simulations, we noticed that symmetry breaking occurs before the theoretically predicted branch termination conditions are met, and no "nose-up" axisymmetric profiles are observed when $\mathrm{Ca}_b < \mathrm{Ca}_l$. Though the detailed mechanism accounting for the symmetry breaking process is out of the scope of the current work, the discrepancies in the critical conditions might be explained in several different ways. First, the symmetry-breaking process is triggered near the upper spherical caps (the bubble "nose" if at a "nose-up" profile, or the "tail" if "nose-down"). However, the theoretical predictions are based on an axisymmetric profile assumption, with the derivation mainly focusing on the uniform film thickness region. Furthermore, we observed that the bubble profile becomes more sensitive to system perturbations when the conditions are closer to the branch termination. Therefore, while the theoretical predictions might provide an "ideal boundary", the system perturbations in experiments or finite resolutions in simulations can account for the early trigger to the symmetry-breaking process.

Here, we report the evidence of such profiles and provide qualitative descriptions of the symmetry-breaking process.

4.2.1. *Asymmetric bubble profiles*

Two symmetry-breaking bubble profiles are shown in figure 6a,b, with figure 6a obtained from an experiment, and figure 6b from a three-dimensional direct numerical simulation (see §3 for the experimental and numerical simulation set-ups). While the experimental figure is captured in the vertical plane, near where the maximum and minimum film thicknesses exist, the simulation figure is plotted at the vertical plane where $y' = 0$, with x', y', z' denoting the coordinates in the 3D numerical simulation. Unlike the asymmetric profiles reported in the literature (e.g. Fabre & Figueroa-Espinoza 2014; Fershtman *et al.* 2017), both the top and bottom caps of the bubble surface are present, and because of this, distinct features are observed about the film profile. Note that the bubble "nose" and "tail" are the sections connected to the uniform film region without and with undulations, respectively. As indicated in figure 6a,b, on the portion of the bubble surface associated with a thick film, the bubble has its nose pointing upward and undulations appears at the bottom. On the portion with a thin film, on the other hand, the bubble has its nose pointing downward and the undulation appearing on the top. Connecting the top and bottom of the bubble forms the bubble centerline, which lies almost vertically and is offset from the tube centerline, towards the direction where the minimum film thickness exists (figure 6a). Based on the numerical solution in figure 6b, the cross-sectional profile of the bubble is shown in figure 6c,d, with the color code in panels (b) and (c) representing the magnitude of the downward fluid velocity normalized by the average fluid velocity U_l. While the simulation begins with an axisymmetric film thickness profile (figure 6d, black dashed circle), once symmetry-breaking occurs, the cross-section of the bubble is no longer circular (red solid curve). For each θ, an axially-uniform film region still exists. The fluid reaches a larger velocity on the bubble surface where the uniform film is thicker, as it encounters less viscous resistance.

4.2.2. *Time-dependent bubble dynamics during symmetry-breaking*

Below, we investigate the transition of the bubble profile from a steady-state axisymmetric shape to an asymmetric shape, resulting from a sudden change in the downward liquid flow rate Ca_l, which forces the bubble to transits from one solution branch to another.

1) Symmetry-breaking from the "nose-up" branch: from $Ca_l = -3.0\times10^{-3}$ *to* -4.0×10^{-3}

We consider the flow configuration with $\mathrm{Bo} = 1.56$. According to the results in figure 5, when moving along the "nose-up" branch towards the left, the theoretical model suggests that the branch terminates before $\mathrm{Ca}_l = -5.0 \times 10^{-3}$ is achieved. On this branch, numerical simulations are run starting from an axisymmetric steady-state profile at $\mathrm{Ca}_l = 0.01$, then gradually decreasing Ca_l (each time until steady state) to move along the branch towards the left. When running three-dimensional simulations, the

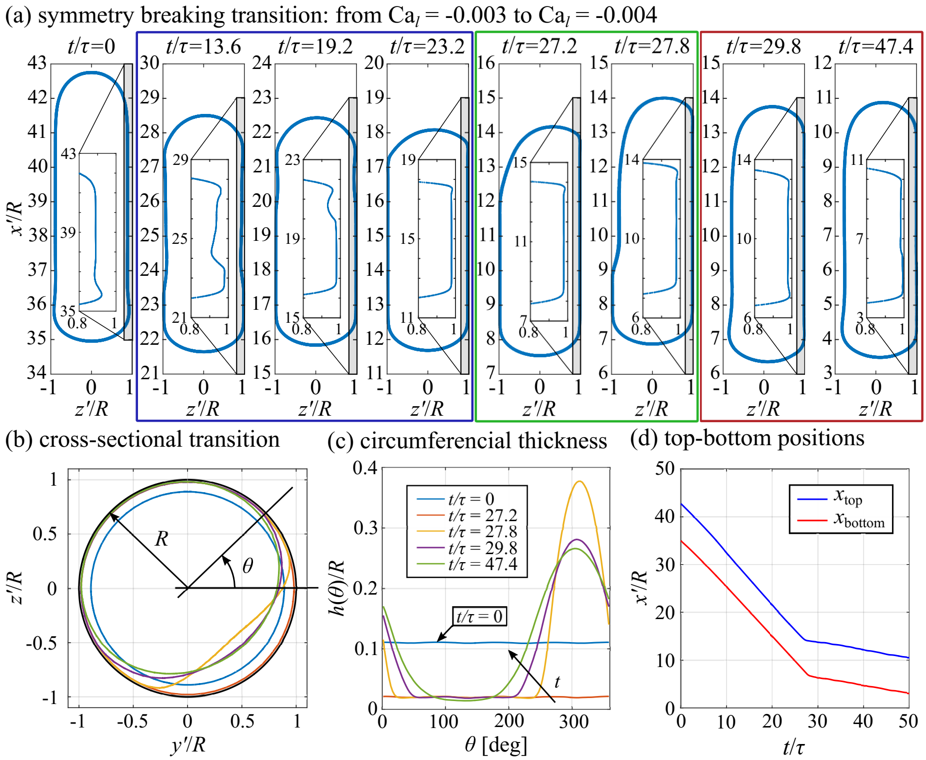

FIGURE 7. Time-dependent evolution from an axisymmetric to a symmetry-breaking bubble profile starting from the "nose-up" branch at Bo $= 1.56$, triggered by a change in Ca$_l$ from Ca$_l$ $= -3.0 \times 10^{-3}$ to -4.0×10^{-3}. (a) Bubble profile at different time stamps in the $y' = 0$ plane. Insets are zoomed-in views of the profiles on the right hand side. The simulation starts at $t/\tau = 0$, with the steady-state profile at Ca$_l$ $= -3.0 \times 10^{-3}$ as the initial condition. Three transitional stages are observed: 1) axisymmetric adjustment (blue box), 2) fast transition to asymmetry (green box), and 3) convergence to a steady-state asymmetric profile (red box). (b) Circumferential film profile measured half way between the bubble top and bottom tips, with the circumferential angle θ measured from $z' = 0$. (c) Circumferential film thickness measurements obtained from panel (b) as a function of θ. (d) The positions of the bubble top and bottom as a function of t/τ, where the bubble speed is significantly decreased after the symmetry-breaking transition.

smallest Ca$_l$ that yields steady-state axisymmetric dynamics is Ca$_l$ $= -3.0 \times 10^{-3}$. A further decrease of the liquid flow rate to Ca$_l$ $= -4.0 \times 10^{-3}$ yields a transition to an asymmetric bubble.

For Ca$_l$ $= -3.0 \times 10^{-3}$, the three-dimensional simulation yields an axisymmetric solution that stays on the "nose-up" branch. At steady state, the bubble sinks with its nose pointing upward, with Ca$_b$ $= -2.2 \times 10^{-3}$ and $b/R = 0.111$. This data point is in the vicinity of the tipping point of the "nose-up" branch (see figure 4e), and the related bubble profile is shown in figure 7a at $t/\tau = 0$, with $\tau \equiv R/U_l$. Using this profile as an initial condition, the background flow rate is decreased to Ca$_l$ $= -4.0 \times 10^{-3}$, which triggers the transition to a symmetry-breaking profile. The bubble transits through three different unsteady regimes as time elapses: (1) axisymmetric adjustment, (2) rapid transition to asymmetry, and (3) convergence to a steady-state asymmetric profile, as shown in figure 7a.

As the simulation begins, at stage 1 (axisymmetric adjustment), a film-thinning wave is generated at the bottom end of the bubble. This wave travels upward and thins the film by generating a new film region (see figure 7a, $t/\tau = 13.6, 19.2$), in a manner similar to Yu *et al.* (2018). This newly generated film smoothly connects to the bottom spherical cap without undulation and has a uniform thickness $b/R = 0.0214$, whose value corresponds to the axisymmetric film thickness on the "nose-down" branch at $\mathrm{Ca}_l = -4.0 \times 10^{-3}$. Thus, the bubble is attempting to transition from the "nose-up" branch to the "nose-down" branch, and this film-thinning wave is adapting to the new background flow rate by generating a downward-pointing nose at the bottom end of the bubble. The initial stage lasts until about $t/\tau = 23.0$, with the thin film surrounding the bubble remaining axisymmetric. However, the top end of the bubble starts to shift sideways slowly from time $t/\tau = 10.0$ on, triggering the instability that gives way to the second stage.

At stage 2 (rapid transition to asymmetry), the asymmetry at the top end triggers a strong film-thickening wave, which travels from the top to the bottom of the bubble in less than one time unit (see figure 7a, $t/\tau = 27.2, 27.8$). This thickening wave only spans a finite range of circumferential angle θ, yet strongly alters the partial profile as it sweeps by, leaving a thick film with a nose pointing upward and a tail pointing downward. The other section of the bubble remains unchanged during this process (see insets of figure 7a), maintaining a thin film thickness at $b/R = 0.0214$, same as in stage 1. Thus, the film-thickening wave is responsible for generating the asymmetric bubble profile, which leads to opposite arrangements of the bubble noses and tails on the thick- and thin film sides of the bubble (see figure 1d and 6a). During stage 1, the bubble sinks at $\mathrm{Ca}_b = -4.2 \times 10^{-3}$. From the end of stage 2 onward, the bubble sinks more slowly at $\mathrm{Ca}_b = -6.0 \times 10^{-4}$ (figure 7d), and the circumferential film thickness profile is strongly asymmetric (figure 7b,c).

At stage 3 (convergence to a steady-state asymmetric profile), capillary effects further adjust the film profile, rounding the film profile corners left from stage 2 (see figure 7b,c, yellow curve) and further thinning the film due to a decrease in speed. As a result, a third thinning wave starts from the bottom of the bubble and propagates towards the top, which is circumferentially localized in the thin film region (figure 7a, $t/\tau = 29.8, 47.4$). This wave propagates at a speed much slower than the previous stages, and the numerical simulation ends before the wave reaches the top of the bubble, since the film becomes too thin ($b/R \lesssim 0.01$) for the computational mesh to capture, i.e., the film eventually dewets. However, based on the dynamics before dewetting, the bubble continues sinking at a constant speed, and the bubble dynamics seems to be converging to a steady-state asymmetric profile, with a very thin film on one side that may eventually dewet.

2) Symmetry breaking from the "nose-down" branch: from $Ca_l = -4.0 \times 10^{-3}$ to -3.0×10^{-3}

When moving along the "nose-down" branch towards the right in figure 5, the theoretical model yields solutions all the way to $\mathrm{Ca}_l = 0$. On this branch, numerical simulations start from an axisymmetric steady-state profile at $\mathrm{Ca}_l = -0.02$, then Ca_l is gradually increased to move along the branch towards the right, each time until steady state. While results from two-dimensional axisymmetric and three-dimensional simulations show excellent agreement up to $\mathrm{Ca}_l = -4.0 \times 10^{-3}$, deviations appear when Ca_l is further increased to $\mathrm{Ca}_l = -3.0 \times 10^{-3}$. The three-dimensional simulation yields a transition to the asymmetric dynamics, whereas the results of the two-dimensional axisymmetric simulations achieve steady-state conditions that stay on the "nose-down" branch, and agree well with the theory. The transition from the "nose-down" branch towards an asymmetric profile is very similar to the previous case and can be categorized in the same three stages; more detail can be found in the supplementary material.

5. Concluding remarks

Theoretical predictions are given for the axisymmetric film profile of an elongated and confined bubble, translating at steady state in a vertically oriented capillary under external flow. The theoretical results are further validated by the experiments and direct numerical simulations. Under the effects of buoyancy and external flow, two solution branches of the axisymmetric film thickness are found. One solution has buoyancy effects mainly driving the bubble motion, and admits a thick film profile with the bubble nose pointing upward; the other solution branch has the external flow effects mainly driving the motion, and admits a thin film profile with the bubble nose pointing downward.

When an external upward flow is applied, a unique shape of a bubble with its nose pointing upward is obtained, and the resultant film thickens with increasing Bo and/or Ca_l. For $\mathrm{Bo} < \mathrm{Bo}_{cr} = 0.842$, the film thickness vanishes as $\mathrm{Ca}_l \to 0^+$. For $\mathrm{Bo} > \mathrm{Bo}_{cr}$, however, the bubble rises spontaneously in a stagnant fluid with a nonzero film thickness. As a result, the bubble can sustain a limited amount of external downward flow and retain the upward nose profile. The larger the Bond number, the larger the range of negative Ca_l that the bubble can tolerate while maintaining this configuration.

The bubble profile with a downward-pointing nose, on the other hand, can only be obtained by applying an external downward flow. While the film thickness increases with the magnitude of the external flow $|\mathrm{Ca}_l|$, it decreases with Bo, since buoyancy serves as resistance in this case. In addition, the film thickness vanishes as $\mathrm{Ca}_l \to 0^-$ regardless of Bo. Combined with the operational range of downward flow for the thick film solution branch, the two solutions overlap for $\mathrm{Bo} > \mathrm{Bo}_{cr}$, resulting in non-uniqueness of the film thickness.

Furthermore, both experiments and three-dimensional simulations show that as the bubble transits between steady states near the tipping points of the two solution branches and attempts to form a new profile with a thinner film, axisymmetry of the bubble profile may be broken. The resultant symmetry-breaking profile is found in the inertialess regime, which differs from the cases documented in the literature at large Bond numbers, as it preserves smooth bubble caps with many of the features that can be described by the classic lubrication theory. Further investigation of this profile can provide valuable insights, enhancing the current understanding of multiphase flows in vertical pipes, and bridging the gap in the literature regarding the dynamics and stability of a bubble in a capillary over a wide range of Bond numbers.

Acknowledgments

We thank NSF for the support via grant CBET-1804863. M.M. acknowledges the use of Athena at HPC Midlands+, which was funded by the EPSRC grant EP/P020232/1, as part of the HPC Midlands+ consortium. L.Z. acknowledges the start-up grant R-265-000-696-133 given by National University of Singapore. We thank the two anonymous referees for helpful comments.

Declaration of Interest

The authors report no conflict of interest.

REFERENCES

Araújo, J. D. P., Miranda, J. M., Pinto, A. M. F. R. & Campos, J. B. L. M. 2012 Wide-ranging survey on the laminar flow of individual Taylor bubbles rising through stagnant newtonian liquids. *Int. J. Multiph. Flow* **43**, 131–148.

Asayesh, F., Zarabadi, M. P. & Greener, J. 2017 A new look at bubbles during biofilm inoculation reveals pronounced effects on growth and patterning. *Biomicrofluidics* **11** (6), 064109.

Aussillous, P. & Quéré, D. 2000 Quick deposition of a fluid on the wall of a tube. *Phys. Fluids* **12** (10), 2367–2371.

Blunt, M. J. 2001 Flow in porous media – pore-network models and multiphase flow. *Curr. Opin. Colloid Interface Sci.* **6** (3), 197–207.

Brackbill, J. U., Kothe, D. B. & Zemach, C. 1992 A continuum method for modeling surface tension. *J. Comput. Phys.* **100**, 335–354.

Bretherton, F. P. 1961 The motion of long bubbles in tubes. *J. Fluid Mech.* **10** (2), 166–188.

Collins, R., De Moraes, F. F., Davidson, J. F. & Harrison, D. 1978 The motion of a large gas bubble rising through liquid flowing in a tube. *J. Fluid Mech.* **89** (3), 497–514.

Dhaouadi, W. & Kolinski, J. M. 2019 Bretherton's buoyant bubble. *Phys. Rev. Fluids* **4** (12), 123601.

Fabre, J. & Figueroa-Espinoza, B. 2014 Taylor bubble rising in a vertical pipe against laminar or turbulent downward flow: Symmetric to asymmetric shape transition. *J. Fluid Mech.* **755**, 485–502.

Feinstein, S. B., Ten Cate, F. J., Zwehl, W., Ong, K., Maurer, G., Tei, C., Shah, P. M., Meerbaum, S. & Corday, E. 1984 Two-dimensional contrast echocardiography. i. in vitro development and quantitative analysis of echo contrast agents. *J. Am. Coll. Cardiol.* **3** (1), 14–20.

Ferrari, A., Magnini, M. & Thome, J. R. 2018 Numerical analysis of slug flow boiling in square microchannels. *Int. J. Heat Mass Tran.* **123**, 928–944.

Fershtman, A., Babin, V., Barnea, D. & Shemer, L 2017 On shapes and motion of an elongated bubble in downward liquid pipe flow. *Phys. Fluids* **29** (11), 112103.

Griffith, P. & Wallis, G. B. 1961 Two-phase slug flow. *J. Heat Trans.* **83** (3).

Hirt, C. W. & Nichols, B. D. 1981 Volume of fluid (VOF) method for the dynamics of free boundaries. *J. Comput. Phys.* **39**, 201–225.

Hu, Y., Bian, S., Grotberg, J., Filoche, M., White, J., Takayama, S. & Grotberg, J. B. 2015 A microfluidic model to study fluid dynamics of mucus plug rupture in small lung airways. *Biomicrofluidics* **9** (4), 044119.

Khodaparast, S., Kim, M. K., Silpe, J. E. & Stone, H. A. 2017 Bubble-driven detachment of bacteria from confined microgeometries. *Environ. Sci. Technol* **51** (3), 1340–1347.

Kotula, A. P. & Anna, S. L. 2012 Probing timescales for colloidal particle adsorption using slug bubbles in rectangular microchannels. *Soft Matter* **8** (41), 10759–10772.

Lamstaes, C. & Eggers, J. 2017 Arrested bubble rise in a narrow tube. *J. Stat. Phys.* **167** (3-4), 656–682.

Li, Z., Wang, L., Li, J. & Chen, H. 2019 Drainage of lubrication film around stuck bubbles in vertical capillaries. *Appl. Phys. Lett.* **115** (11), 111601.

Lu, X. & Prosperetti, A. 2006 Axial stability of Taylor bubbles. *J. Fluid Mech.* **568**, 173–192.

Magnini, M., Ferrari, A., Thome, J. R & Stone, H. A. 2017 Undulations on the surface of elongated bubbles in confined gas-liquid flows. *Phys. Rev. Fluids* **2** (8), 084001.

Magnini, M., Khodaparast, S., Matar, O. K., Stone, H. A. & Thome, J. R. 2019 Dynamics of long gas bubbles rising in a vertical tube in a cocurrent liquid flow. *Phys. Rev. Fluids* **4** (2), 023601.

Magnini, M. & Matar, O. K. 2020 Numerical study of the impact of the channel shape on microchannel boiling heat transfer. *Int. J. Heat Mass Tran.* **150**, 119322.

Martin, C. S. 1976 Vertically downward two-phase slug flow. *J. Fluids Eng.* **98** (4), 715–722.

Nicklin, D. J. 1962 Two-phase flow in vertical tubes. *Inst. Chem. Engr.* **40** (1), 61–68.

Polonsky, S., Barnea, D. & Shemer, L. 1999 Averaged and time-dependent characteristics of the motion of an elongated bubble in a vertical pipe. *Int. J. Multiph. Flow* **25** (5), 795–812.

Quéré, D. 1999 Fluid coating on a fiber. *Annu. Rev. Fluid Mech.* **31** (1), 347–384.

Taitel, Y., Barnea, D. & Dukler, A. E. 1980 Modelling flow pattern transitions for steady upward gas-liquid flow in vertical tubes. *AIChE Journal* **26** (3), 345–354.

Thulasidas, T. C., Abraham, M. A. & Cerro, R. L. 1995 Bubble-train flow in capillaries of circular and square cross section. *Chem. Eng. Sci.* **50** (2), 183–199.

Uhlendorf, V. & Hoffmann, C. 1994 Nonlinear acoustical response of coated microbubbles in diagnostic ultrasound. In *Ultrasonics Symposium Proceedings.*, , vol. 3, pp. 1559–1562. IEEE.

Yu, Y. E., Khodaparast, S. & Stone, H. A. 2017 Armoring confined bubbles in the flow of colloidal suspensions. *Soft Matter* **13** (15), 2857–2865.

Yu, Y. E., Zhu, L., Shim, S., Eggers, J. & Stone, H. A. 2018 Time-dependent motion of a confined bubble in a tube: Transition between two steady states. *J. Fluid Mech.* **857**.

Zhou, G. & Prosperetti, A. 2019 Violent expansion of a rising Taylor bubble. *Phys. Rev. Fluids* **4** (7), 073903.